Optimizing third-harmonic generation at terahertz frequencies in graphene

Ibraheem Al-Naib, Max Poschmann, and Marc M. Dignam
Department of Physics, Engineering Physics and Astronomy, Queen's University, Kingston, Ontario K7L 3N6, Canada
(Received 12 March 2015; revised manuscript received 20 April 2015; published 11 May 2015)

We model third-harmonic generation in doped monolayer graphene at terahertz frequencies by employing a nearest-neighbor tight-binding model in the length gauge. We show that for a given incident-field amplitude there is an optimum Fermi level that maximizes the emitted third-harmonic field. The optimum Fermi level depends very strongly on the incident-field amplitude as well as on the scattering time and increasing either enhances the third-harmonic response. We consider the general case of Fermi-level-independent scattering as well as three different scattering mechanisms that are Fermi-level dependent: phonon, long-range impurity, and short-range impurity scattering. For each case, we determine the optimal Fermi level as well as the amplitude of the optimized third-harmonic response for single-cycle incident fields with central frequencies of 1 THz and amplitudes in the range of 25–75 kV/cm. We find that although nonlinear processes beyond third order suppress third-harmonic generation, we still obtain third-harmonic amplitudes as large as 1.6% of the fundamental of the transmitted field.

DOI: 10.1103/PhysRevB.91.205407 PACS number(s): 72.20.Ht, 72.80.Vp, 42.65.−k, 73.50.Fq

I. INTRODUCTION

Graphene, a two-dimensional allotrope of carbon, has a number of features that make it an attractive nonlinear system to study [1–4]. These include a tunable Fermi level, which can be adjusted via an applied gate voltage [5,6], and more importantly a linear dispersion relation near the Dirac point [7,8]. This linear dispersion and the accompanying constant Fermi velocity has led to the prediction of the generation of high harmonics in graphene [1]. Application of an electric field results in a rate of change in the crystal momentum within a given band that depends linearly on the applied electric field in the usual way. However, because the electron dispersion in graphene is linear in k near the Dirac points, the electron velocity is independent of the crystal momentum. Thus, the current experiences saturation when, due to the application of a strong terahertz (THz) field, most of the electrons move to one side of the Dirac point in k space. This leads to a suppression in the temporal peaks of the current density, i.e., "clipping" of the current, which in turn results in the generation of odd harmonics in the current and transmitted electric field.

Third-order nonlinearities in graphene have been investigated theoretically and experimentally across the electromagnetic spectrum [1,2,9–17]. In the optical regime, different third-order processes have been measured, such as four-wave mixing [2] and third-harmonic generation [18,19]. However, there have been inconsistencies in the values for the extracted effective susceptibilities with results depending strongly on the measurement method, operating frequency, and sample preparation [15]. At terahertz frequencies, high harmonic response in graphene has been predicted theoretically [1,9,10,12], but the only reported experimental evidence of harmonic generation has been in a 45-layer-thick sample [20]. There has been no indication of harmonic generation in *monolayer* graphene, although a nonlinear suppression of the conductivity has been observed [21]. Hence, it is important to understand why harmonic generation has not generally been observed and to investigate the effects of different system and experimental parameters on the efficiency of high harmonic generation so as to determine the conditions under which a third-harmonic response may best be observed. The nonlinear response, of course, depends on the amplitude of the incident electric field. However, it is less obvious how the Fermi level in the graphene sample and scattering times of the charge carriers in the sample will affect harmonic generation.

In this paper, we develop a theoretical model based on the density-matrix formalism in the length gauge to calculate the nonlinear THz response of graphene. We employ this model to examine the dependence of third-harmonic generation on the amplitude of the incident electric field, the Fermi level, and the scattering time of the charge carriers in a monolayer graphene sample. Although some previous theoretical investigations [9,12] have ignored scattering effects, we find that the third-harmonic amplitude is strongly affected by scattering. Because scattering times in graphene are only on the order of tens of femtoseconds, it is very important to include scattering processes in any model of the THz response of graphene. This is in contrast to models at optical frequencies where neglecting scattering is often a reasonable approximation [15]. There have been extensive theoretical and experimental studies on carrier scattering in graphene [8,22–25]. In principle, there are four mechanisms of carrier scattering that can be important in graphene: phonon scattering, long-range impurity scattering, short-range impurity scattering, and carrier-carrier scattering. In this paper, we first optimize the Fermi level for a given Fermi-level-independent scattering mechanism and then optimize it when a different scattering mechanism is dominant. In the latter case, we account for the different Fermi-level dependence of the scattering time for three different scattering mechanisms: phonon, long-range impurity, and short-range impurity. We examine each scattering mechanism separately and optimize the Fermi level for strongest third-harmonic response for a range of field amplitudes of 25–75 kV/cm. We find that for any combination of incident electric-field amplitude and sample scattering time (or dominant scattering mechanism) there is an optimal Fermi level for which the transmitted third-harmonic response generated by graphene in the terahertz regime will be strongest. We find that the

amplitude of the generated third-harmonic field can be as large as 1.6% of the fundamental of the transmitted field. These results will be useful in guiding further experimental studies at high-field amplitudes and tunable Fermi levels towards efficient and detectable third-harmonic generation from monolayer graphene. Moreover, they also help explain why third-harmonic generation has not been experimentally observed from monolayer graphene to date.

The paper is organized as follows. In Sec. II, starting with the tight-binding method to obtain interaction matrix elements in the length gauge, we present a brief derivation of our theoretical model to calculate the intraband current density and the transmitted field. In Sec. III, we introduce the three different scattering mechanisms and show the scattering time versus Fermi-level dependencies considered here. In Sec. IV, the numerical simulations are presented with both Fermi-level-independent and Fermi-level-dependent scattering. Finally, the conclusions are presented in Sec. V.

II. THEORY

We employ a nearest-neighbor tight-binding model for the band structure of graphene [8,26]. The tight-binding expression for the Bloch states is as follows:

$$\Psi_{[c,v]\mathbf{k}}(\mathbf{r}) = F\sum_{\mathbf{R}} e^{(i\mathbf{k}\cdot\mathbf{R})}[\psi_p(\delta\mathbf{r}_A) + C\psi_p(\delta\mathbf{r}_B)], \quad (1)$$

where c and v indicate conduction and valence bands, F is a normalization constant, $C = \sigma_{c,v}e^{-i\chi(\mathbf{k})}$, $\sigma_{c,v} = \{-1,1\}$, $\chi(\mathbf{k}) = \arg(1 + e^{-i\mathbf{k}\cdot\mathbf{a}_1} + e^{-i\mathbf{k}\cdot\mathbf{a}_2})$, $\mathbf{a}_1$ and $\mathbf{a}_2$ are the primitive Bravais lattice vectors, $\psi_p(\mathbf{r})$ is the wave function of a carbon $2p_z$ orbital electron, $\delta\mathbf{r}_{A,B} \equiv \mathbf{r} - \mathbf{R} - \mathbf{r}_{A,B}$, where $\mathbf{r}_A$ and $\mathbf{r}_B$ are basis vectors for the A and B atoms within the graphene unit cell, and the sum is over the Bravais lattice vectors $\mathbf{R}$. We employ the length-gauge Hamiltonian [27],

$$H = H_0 - e\mathbf{r}\cdot\mathbf{E}(t), \quad (2)$$

where H_0 is the unperturbed Hamiltonian of graphene, $e = -|e|$ is the electron charge, $\mathbf{r}$ is the electron position vector, and $\mathbf{E}(t)$ is the THz electric field at the graphene layer, which is equal to the transmitted field. The length gauge has been employed rather than the velocity gauge because it has been shown in previous works [27–29] that the length gauge does not result in the unphysical divergences for the nonlinear response when a finite set of energy bands is employed.

Following the Aversa and Sipe approach [27], the time dependence of the density operator in the conduction and valence bands including interband and intraband transitions as well as scattering within and between these bands may be determined. Carrier dynamics in graphene under stimulation by an electric field involve both interband transitions (between bands) and intraband transitions (within a band). These two types of transitions are illustrated in Fig. 1. In previous work [14], we have included interband and intraband transitions in a density-matrix approach. However, because we are only considering n-doped graphene in this paper, interband transitions play a negligible role in the response and can be safely omitted (as we will demonstrate below). Thus for most of the calculations presented below, a simplified model involving only intraband transitions is used.

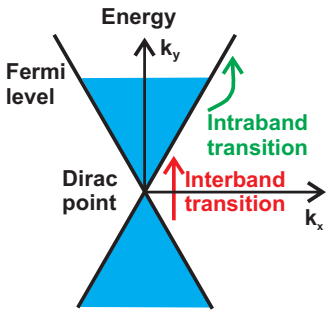

FIG. 1. (Color online) Diagram of the dispersion relation in graphene near the Dirac point showing the linear dispersion, Dirac point, Fermi level due to doping, and both intraband and interband transitions.

In treating the scattering, we employ the relaxation-time approximation, which assumes that as the carrier populations scatter, they relax to a Fermi-Dirac distribution,

$$f_c = \left[\exp\left(\frac{E - E_F}{k_B T}\right) + 1\right]^{-1}, \quad (3)$$

where E is the electron energy, E_F is the Fermi energy, k_B is the Boltzmann constant, and T is the temperature. Thus, the time dynamic equation for the electron-density operator is given by [14]

$$\frac{d\rho_{cc}(\mathbf{k})}{dt} = -\frac{e\mathbf{E}(t)}{\hbar}\cdot\nabla_{\mathbf{k}}\rho_{cc}(\mathbf{k}) - \frac{\rho_{cc}(\mathbf{k}) - f_c(\mathbf{k},t)}{\tau}, \quad (4)$$

where τ is the population scattering time, which is considered to be independent of energy. The intraband current density, which in this case is the total surface current density $\mathbf{J}_s$ in the graphene sample, is then given by

$$\mathbf{J}_s(t) = \frac{4ev_F}{A}\sum_{\mathbf{k}} \rho_{cc}(\mathbf{k},t)\widehat{\mathbf{k}}, \quad (5)$$

where A is the normalization area of the graphene sheet and the sum is only over the region close to one of the Dirac points, v_F is the Fermi velocity, and $\widehat{\mathbf{k}}$ is the unit vector in k space where the origin is at one of the Dirac points.

To determine the response of the system, the electric field transmitted through a layer of graphene on the interface between the air and a substrate is required. Taking the index of refraction of the substrate to be n, the transmitted field $[\mathbf{E}_t(t)]$ is given by

$$\mathbf{E}_t(t) = \frac{2\mathbf{E}_i(t) - \eta_0\mathbf{J}_s(t)}{n+1}, \quad (6)$$

where $\mathbf{E}_i(t)$ is the incident terahertz field and η_0 is the impedance of free space.

III. CARRIER SCATTERING

One of the challenges in optimizing the third-harmonic response with respect to the Fermi level and scattering time is the possible dependence of the scattering time on carrier density and thus on the Fermi level. Numerous experimental [25] and theoretical [23,30–32] studies have sought to calculate or measure the dependence of the scattering time (or conductivity

or carrier mobility) as a function of carrier density and have come to a variety of conclusions. There are four important sources of carrier scattering in graphene: phonon scattering, long-range impurity scattering, short-range impurity scattering, and carrier-carrier scattering [8,23,25,32,33]. For the doping levels considered in this paper, the carrier-carrier scattering time is expected to be greater than 100 fs for an electron with an energy that is less than 1 eV above the Fermi energy [23]. Thus, for the doping levels considered in this paper, it is expected that the average electron-electron scattering time will be considerably more than 100 fs, which is somewhat longer than the other scattering times. Hence, for simplicity, we have neglected the electron-electron scattering as it is not expected to qualitatively change the results.

In this section, we give a brief description of each of the first three types of scattering mentioned above and examine the scattering times over the range of Fermi levels that are used in the simulations. In the next section, we will calculate the dependence of the generated third harmonic on the Fermi level and incident-field amplitude for different scattering mechanisms. Because the impurity-scattering times depend sensitively on the impurity density, each sample will have a different dependence on temperature and Fermi level. Thus, rather than trying to combine the effects of all three scattering mechanisms in our nonlinear simulations, we treat each one separately. Because all samples will have phonon scattering, one can then interpret the results using the different scattering mechanisms from samples in which one of the three mechanisms dominates.

A. Phonon scattering

Lattice vibrations lead to a phonon-scattering channel that is unavoidable and can dominate transport near room temperature in very clean samples [8]. The key data that we employ to model the phonon-scattering mode is from Chen *et al.* [25], who provided experimental results for the conductivity (σ) versus gate voltage data for a number of different samples of graphene on a SiO_2 substrate. As these data are dominated by phonon scattering rather than impurity scattering, it is thought that they must represent a high quality clean sample. The samples discussed later in which scattering is dominated by impurities almost certainly experience the same phonon scattering observed here but also a larger degree of impurity scattering. Therefore, it is not surprising that this phonon-dominated sample possesses the longest scattering times.

For our simulations, we use the data for sample 1 in Fig. 1(c) of Chen *et al.* [25] and use their Eq. (2b) to fit the data [here Eq. (7)], which fits their measurements somewhat better than the alternative models they present. This semiempirical equation contains contributions from longitudinal acoustic phonons and remote interfacial phonon scattering by the polar optical phonons of the SiO_2 substrate. Using this, our expression for the inverse of the dc conductivity is given by

$$\sigma^{-1}(N,T) = \sigma_0^{-1}(N) + \sigma_A^{-1}(T) + \sigma_B^{-1}(N,T), \qquad (7)$$

where N is the carrier density, T is the temperature, σ_0^{-1} is the residual resistivity at low temperatures, σ_A^{-1} is the resistivity due to acoustic phonon scattering, and σ_B^{-1} is a single Bose-Einstein distribution fitting parameter that is most likely related to interfacial phonon scattering [25].

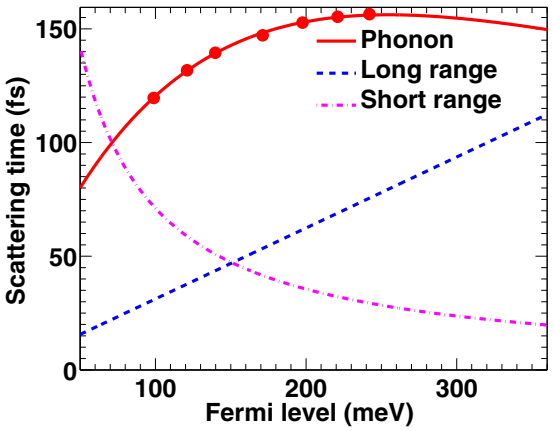

FIG. 2. (Color online) Three models for scattering time as a function of Fermi level: phonon dominated (with dots represent the experimental values [25]), long-range impurity dominated, and short-range impurity dominated.

Now, using the Drude model, the linear dc conductivity is given by

$$\sigma = \frac{e^2 E_F}{\hbar^2 \pi}\tau, \qquad (8)$$

where τ is the electron-phonon scattering time that we wish to determine and the Fermi energy is related to the carrier density by $E_F = v_F \hbar\sqrt{\pi N}$.

Using Eq. (8) and the expression for σ in terms of the components σ_0, σ_A, and σ_B, we can examine each component and determine an accurate function for scattering time τ. In order to obtain σ_0, we have fit the experimental data to a power-law equation. The final result is shown as the solid red curve in Fig. 2 along with the experimental data (dots) for a Fermi-level range between 50 and 360 meV. The corresponding scattering time increases from 80 fs to almost 155 fs.

B. Charged long-range impurity scattering

Charged long-range impurity scattering due to impurities in the substrate has been proposed in order to explain the linear behavior of graphene conductivity versus the carrier density concentration in low carrier density samples [23] and successfully explains several transport experiments [34–36]. As discussed by Hwang and Das Sarma [23], in samples that are dominated by charged impurity scattering, due to screening by the carriers in the graphene, the scattering time increases with Fermi energy and is given by

$$\tau = \frac{E_F}{2\pi n_i \hbar v_F^2 I_c}, \qquad (9)$$

where n_i is the impurity number density and I_c is a factor that is approximately 0.053 for graphene on SiO_2 [23]. The impurity concentration depends very much on the graphene substrate. In order to keep our scattering times on the same order as that found at room temperature due to phonon scattering, we take our charged impurity concentration to be $1.5 \times 10^{12}/\text{cm}^2$, which is similar to the one reported in Ref. [37] and leads to

scattering times similar to those found in the recent graphene literature [30–32]. The dependence of the charged impurity-scattering time as a function of the Fermi energy for the above impurity density is plotted as the dashed blue line in Fig. 2.

C. Short-range impurity scattering

We finally consider short-range impurity scattering arising due to disorder in the graphene itself. From Hwang and Das Sarma [23], for short-range impurities, the expression for the scattering time is

$$\tau = \frac{\pi \hbar^3 v_F^2}{2 n_i V_o^2 I_n E_F}, \tag{10}$$

where n_i is the impurity number density, V_o is the scattering potential, and I_n is a dimensionless factor that is approximately 0.03 for graphene on SiO_2. Following Hwang and Das Sarma [23], we take $V_o = 1\ \text{keV}\,\text{Å}^2$, and to bring these scattering times into the same range as the phonon- and long-range scattering times discussed above, we take the impurity concentration to be $n_i = 2 \times 10^{12}/\text{cm}^2$, which is consistent with values found in the literature [38,39]. For this impurity density, the short-range impurity-scattering time is plotted as the dashed-dotted curve in Fig. 2.

IV. RESULTS

To perform our simulations, we discretize k in Eq. (4) on a square grid. We solve the coupled dynamic equations using the Runge-Kutta algorithm with an adaptive time step. The values for the density matrix as a function of time at each point in k are used to evaluate Eq. (5), the result of which is used to calculate the transmitted field via Eq. (6). For simulations in which interband terms are excluded, a grid size of 401×401 cells with a maximum energy of 2.5 eV was required for convergence of the transmitted field. In all simulations, we make the approximation that the electron dispersion relation is exactly linear with a Fermi velocity of $v_F = 1.0 \times 10^6$ m/s. Using the tight-binding expression for the full dispersion, we find that this linear expression for the dispersion is accurate up to energies of about 900 meV at which energy it deviates by less than 5.6% from the linear relation. This also means that for energies below 900 meV, the electron group velocity differs by less than 12% from v_F. To ensure that we stay within the linear regime, in all of our simulations, we choose the maximum THz fields and Fermi energies such that no more than 10% of all charge carriers ever occupy states with energies above 900 meV.

In this paper, we aim to replicate conditions easily achievable in a laboratory to best provide useful guidance to experimentalists. The system we model is a monolayer of graphene placed on top of a fused quartz substrate, which has a refractive index of approximately 1.9 at terahertz frequencies [40–42]. The temperature of the system is taken to be 300 K, and the sample is assumed to be in vacuum so as to avoid possible effects due to background gases [43]. In all cases, the THz pulse is normally incident to the graphene and is a 1 THz sine wave with a Gaussian envelope with a full width at half maximum of 1 ps and an amplitude of E_o [44]. This pulse was chosen because it is typical of the single-cycle pulses

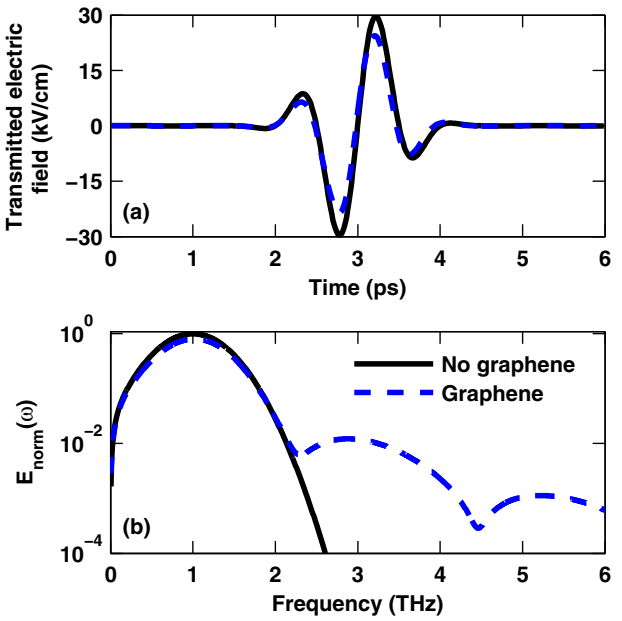

FIG. 3. (Color online) (a) Transmitted temporal signal and (b) the corresponding normalized amplitude spectra, $E_{\text{norm}}(\omega)$ for $E_o = 50$ kV/cm, Fermi level of 240 meV, and scattering time of 156 fs without (black solid line) and with (dashed blue line) graphene present.

that are often obtained experimentally [45,46]. The duration of each simulation is 6 ps with the pulse at the center of the simulation time window. The electric field of the transmitted pulse just after the air-quartz interface is shown in Fig. 3(a) with (dashed line) and without (solid line) the graphene layer. The Fourier transforms of both these fields are shown in Fig. 3(b) where the Fourier amplitude of the transmitted field is normalized to the amplitude of the transmitted field at the fundamental frequency of 1 THz for the case when the graphene is not present. Thus, the normalized transmitted amplitude spectrum is defined as

$$E_{\text{norm}}(\omega) \equiv \left| \frac{E_t(\omega)}{E_t^o(\omega_o)} \right|, \tag{11}$$

where $\omega_o/2\pi = 1$ THz and $E_t^o(\omega)$ is the field transmitted through bare SiO_2. As can be seen, in addition to the small decrease in the amplitude of the field at the fundamental, we see the clear presence of THz components at both 3 and 5 THz. In the following, we concentrate on the generated third-harmonic field.

A. Fermi-level-independent scattering

Before considering the third-harmonic generation results using the above three models of scattering (which depend on the Fermi level), we first present the results of simulations where the scattering time is *independent* of the Fermi level. Although generally speaking both interband and intraband dynamics will occur in the graphene [14], the interband dynamics will play a very small role if the Fermi level is sufficiently high such that the interband transitions are largely Pauli blocked. Thus, in our simulations, we take $E_F \geqslant 50$ meV, which is much greater than the average photon

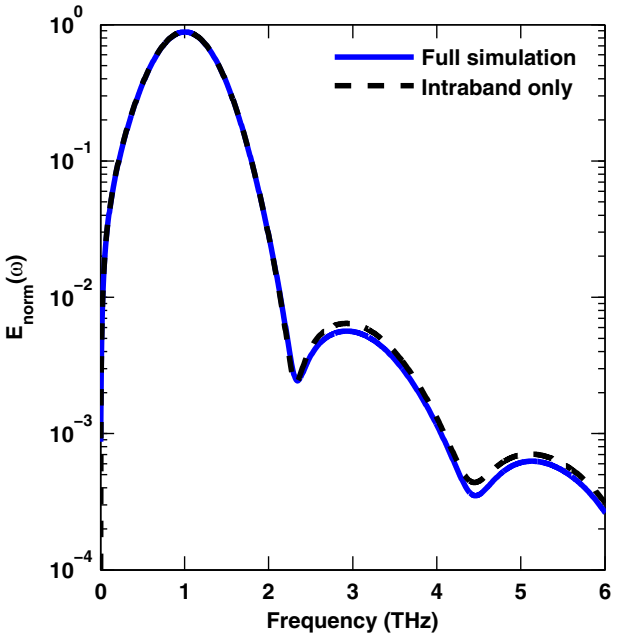

FIG. 4. (Color online) The calculated normalized transmitted THz field $E_{\rm norm}(\omega)$ as calculated using the full simulation (solid line) and using a simulation that only includes intraband motion (dashed line) for $E_o = 50$ kV/cm, a Fermi energy of 185 meV, and a scattering time of 65 fs.

energy of only 4.14 meV for our 1 THz pulse. To confirm that we can safely neglect the interband transitions, we have performed a full simulation including both interband and intraband dynamics using the theoretical model we presented in Ref. [14] alongside a simulation that includes the intraband dynamics only. The results of the normalized transmitted field spectra $E_{\rm norm}(\omega)$, found using these two different simulations, are shown in Fig. 4 for $E_o = 50$ kV/cm, a scattering time of 65 fs, and a Fermi level of 185 meV. We have chosen this value for the Fermi energy because (as we will show towards the end of this sub-section) it is close to the optimized values for this field amplitude and scattering time. As can be seen, excluding the interband current leads to an overestimate of the third-harmonic amplitude of only ∼12%.

Figure 5 shows the calculated density distribution near the Dirac point during excitation for $E_o = 50$ kV/cm, a Fermi level of 185 meV, and a scattering time of 65 fs at the time $t = 2.75$ ps when the carriers are at their extreme displacement to the right in k space. One can see that these carriers are driven significantly away from the Dirac point, which is a requirement to create significant current clipping and therefore third-harmonic generation. However, this creates a certain amount of unoccupied states at low energies near the Dirac point, opening the way to interband transitions. Although these interband transitions do occur, our simulation shows that the interband current is at least two orders of magnitude lower than the intraband current, and as discussed above the effect of these transitions on third-harmonic generation is not significant in the cases studied here.

We examined a variety of different cases where one would expect the interband transitions to be most important, i.e., those where the Fermi energy is low and the field is high;

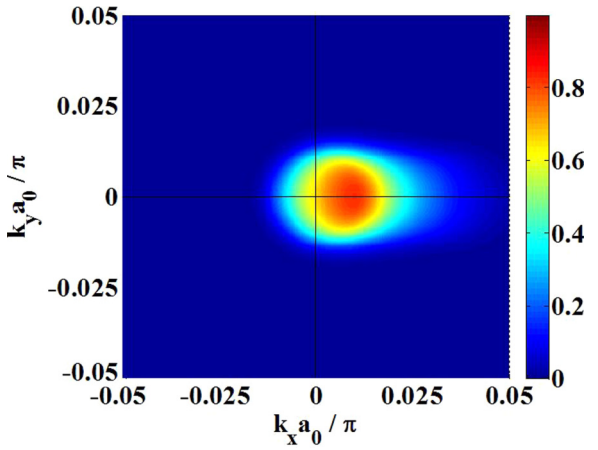

FIG. 5. (Color online) Plot of the electron density in k space at the time when carriers have been moved to their maximum displacement to the right for the $E_o = 50$ kV/cm field, a 185 meV Fermi level, and a 65 fs scattering time.

in all cases, the exclusion of the interband current only leads to a small overestimate in the third harmonic that is at most 12%. The effect of the interband transitions on the nonlinear response of doped graphene was also noted by Ishikawa [12]. The reduction in the nonlinearity due to interband transitions occurs because interband carrier injection increases the carrier density, which in turn increases the intraband current and thus reduces the clipping effect. The inclusion of the interband response in our simulations increases the simulation time by about a factor of 200, increasing the time required for a one run case from a few minutes to a few days. Because we need to perform hundreds of simulations to obtain the optimized Fermi energy of each field amplitude and scattering time, the results that we present in the rest of the paper are calculated using simulations that only include the intraband response. To minimize the effect of omitting interband transitions, we limit the field amplitude, scattering time, and Fermi level such that interband effects are below 12%.

In Fig. 6 we plot $E_{\rm norm}(3\omega_o)$ as a function of the Fermi energy and the scattering time for an incident-field amplitude of $E_o = 50$ kV/cm. Also shown in the plot (via the black dots joined by a solid line) is the optimum Fermi energy for a given scattering time. We clearly see that for samples with longer scattering times, it is preferable to have a higher Fermi level. This trend arises because, although a higher Fermi energy leads to a larger current, if the Fermi energy is too high, then only a small fraction of the carriers will be driven to the other side of the Dirac point in k space, and so the clipping that leads to the third harmonic will be minimal. Increasing the scattering time results in an increase in the distance that the average carrier is driven in k space, which means that the optimum Fermi energy increases with scattering time.

We have found that for all electric-field amplitudes and scattering times considered, an optimal Fermi level can be found for third-harmonic generation. However, rather than present a systematic study of these results for different field amplitudes for our density-independent scattering time, we now turn instead to the results for the three different models of carrier scattering.

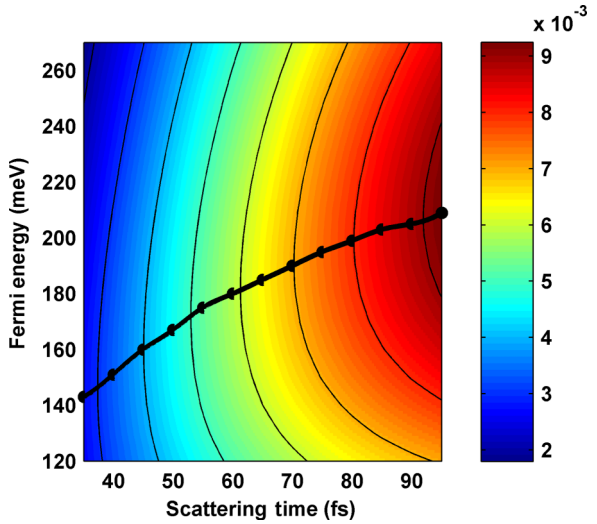

FIG. 6. (Color online) Normalized third-harmonic amplitude $E_{\text{norm}}(3\omega_o)$ as a function of the scattering time and Fermi level for an incident-field amplitude of $E_o = 50$ kV/cm. The black circles indicate the Fermi energy that yields a maximum third harmonic for a given scattering time.

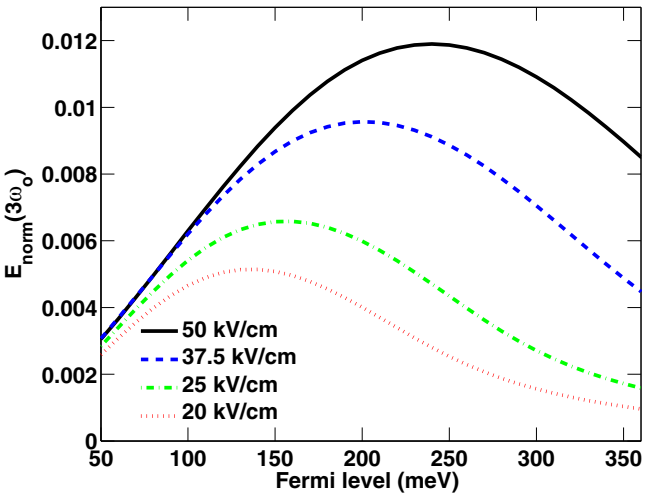

FIG. 7. (Color online) Simulation results from the fit to the phonon-dominated scattering data (see Fig. 2) for the normalized third-harmonic field amplitude as a function of Fermi level for a range of incident-field amplitudes E_o (top to bottom: 50, 37.5, 25, and 20 kV/cm).

B. Fermi-level-dependent scattering

Having observed that in the absence of any relationship between Fermi level and scattering time there is always a particular Fermi level for which third-harmonic THz generation is optimal, it is natural to extend the discussion to the more realistic case in which there is *dependence* of the scattering time on the Fermi level. As discussed in Sec. III of this paper, we have performed nonlinear simulations for graphene dominated by one of three types of scattering: phonon, long-range impurity, and short-range impurity. In this section we investigate whether there still exists an optimal Fermi level at a given field amplitude for each model of scattering and how the optimization is affected by the scattering time function. In general, for samples containing a significant density of short-range and long-range impurities, the scattering in the sample will be dominated by short-range scattering at high Fermi levels and by long-range scattering at low Fermi levels [8]. However, to allow for the possibility that a sample may contain a much higher density of one type of impurity than the other and therefore be dominated at all Fermi levels by the corresponding scattering mechanism, we have considered all scattering modes *separately* for Fermi levels over the range of 50–360 meV. We start with the case of phonon-dominated scattering. In Fig. 7, we plot the normalized third-harmonic field amplitude as a function of the Fermi energy for four different incident-field amplitudes. We note that for all field amplitudes, there is an optimal Fermi energy and that this energy increases with increasing field amplitude as expected. Moreover, we note that choosing the optimum Fermi level is very important. For example, a 150 meV deviation in the Fermi energy from the optimum value can reduce the third-harmonic response by 50% or more.

In order to observe third-harmonic amplitudes, such as shown in Fig. 7 experimentally, a quite high dynamic range (defined as the ratio of the frequency-dependent signal amplitude to the detected noise floor [47,48]) is required. For the phonon-dominated mechanism and 50 kV/cm incident field, the maximum normalized third-harmonic amplitude peaks at 11.9×10^{-3} (i.e., 38.5 dB below the fundamental) for a Fermi level of approximately 240 meV. The third-harmonic amplitude decreases to about 5.6×10^{-3} at a 90 meV Fermi level, which is 6.5 dB below the peak. Hence, a dynamic range larger than 45 dB becomes necessary to observe such third-harmonic signals. Such a dynamic range is achievable as presented in Ref. [20] where the third-harmonic level was measured successfully in multilayer graphene. Moreover, this perhaps explains why the third harmonic was not seen in Ref. [21] where dynamic range was only about 23 dB. Therefore, accurate tuning of the Fermi level as well as a quite high experimental dynamic range are rather critical in order to observe strong third-harmonic generation in graphene.

Rather than plotting the third-harmonic field as a function of Fermi energy for different incident-field amplitudes for the other two scattering mechanisms, we now present the optimized Fermi energy and the resultant optimized normalized third-harmonic amplitude for all three scattering mechanisms in Figs. 8(a) and 8(b), respectively, as a function of the incident-electric-field amplitude. As was shown in Fig. 6, longer scattering times result in stronger third-harmonic responses. Thus, for each scattering mechanism, for a given incident-field amplitude, the optimal Fermi level curve is skewed towards Fermi levels that correspond to longer scattering times. This results in a much lower optimum Fermi energy for samples dominated by short-range impurity scattering than for those dominated by either phonon or charged impurity scattering. Note that for the range of field amplitudes considered, the optimal Fermi energy never exceeds 360 meV but can be as low as 80 meV for samples which are dominated by short-range impurities. Since the scattering time for the long-range impurity-dominated samples is much less than the phonon-dominated scattering scenario, the calculations

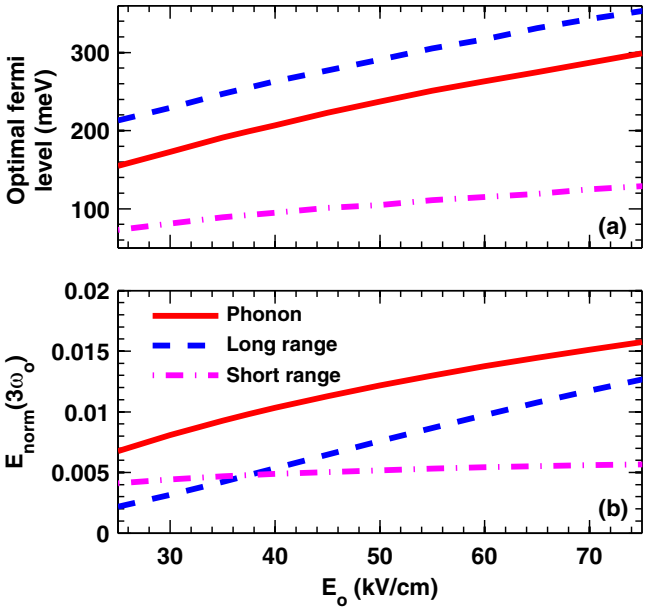

FIG. 8. (Color online) (a) Optimal Fermi level and (b) normalized third-harmonic field amplitude as a function of the incident-field amplitude for the three scattering models.

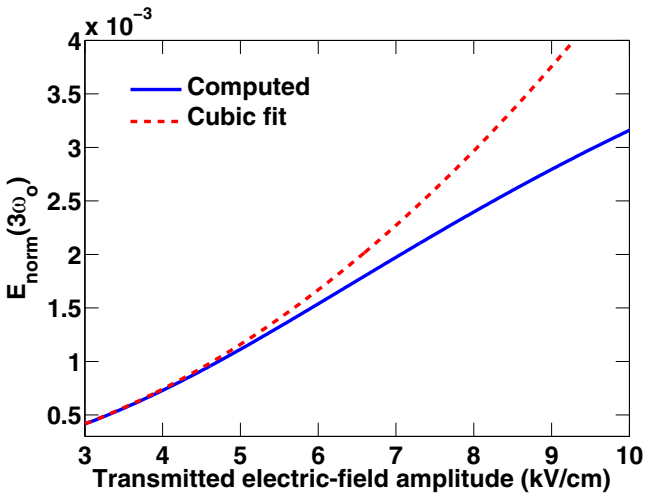

FIG. 9. (Color online) Dependence of the normalized third-harmonic amplitude on the transmitted field amplitude for a short-range scattering model with a Fermi level of 105 meV and a scattering time of 68 fs.

revealed a higher optimized Fermi level for this mode. As the scattering times for the phonon-dominated scattering scenario are longer than for the other two scenarios, the resulting third-harmonic amplitude is highest as shown in Fig. 8(b).

The short-range impurity-scattering case was the only case considered for which the scattering time decreased with increasing Fermi level. This leads to a number of differences between this case and the other two. In general, the observed trend in all cases is that as the incident-field amplitude is increased, the optimal Fermi level and the third-harmonic response also increased. For the phonon and long-range samples, the increase in the Fermi level leads to increased scattering time, leading to a steep increase in third-harmonic response. However, for the short-range case, the increase in the third-harmonic response with field amplitude is much weaker due to the decrease in scattering time as the Fermi energy increases.

In view of the results presented in Fig. 8(b), it is evident that the required dynamic range is significantly less if the sample is clean, i.e., phonon dominated. For instance, at an incident field of 75 kV/cm, the third-harmonic amplitude power is −35.9 dB, whereas it is −44.9 dB for short-range impurity scattering. Having said that, the required dynamic range might be much higher if the Fermi level is not tuned to the optimum values shown in Fig. 8(a). Moreover, it is worth mentioning that recent studies [49,50] have shown that the scattering time in certain samples of graphene decreases when the electric-field amplitude increases. Such a decrease would lead to a reduction in the third-harmonic level for a given field amplitude, and hence a higher field would be required to achieve the same third-harmonic level. Because this field dependence is sample and Fermi-level dependent, for simplicity we have not included it in the analysis presented here but leave it for future work.

When scattering time and Fermi level are held constant, if the process that generates the third harmonic is a purely $\chi^{(3)}$ effect, then the amplitude of the generated third-harmonic field should increase as the cube of the incident THz field. When the Fermi level is optimized to generate the largest third-harmonic response at each incident-field amplitude, one might expect that the third-harmonic response would thus increase at least cubically with the incident field and perhaps even more rapidly due to the selection of optimal Fermi level at each field amplitude. This would thus lead to a quadratic dependence of the normalized third-harmonic amplitude on the incident-field amplitude. It is clear, however, that this is not what is seen for any of the scattering mechanisms for the normalized third-harmonic fields plotted in Fig. 8(b).

To explain the subcubic response, we have analyzed the third harmonic for the short-range scattering mode starting from low transmitted field amplitudes of 3 kV/cm up to 10 kV/cm. In Fig. 9, we plot the normalized third-harmonic amplitude as a function of transmitted electric field for a Fermi energy of 105 meV and a scattering time of 68 fs. The optimal incident-field amplitude for this combination is 50 kV/cm, which is much higher than the upper value selected for this sweep. For a purely third-order response, $E_t(3\omega_o)$ should depend cubically on the transmitted field amplitude; we fit such a cubic response to the calculated results at low fields in Fig. 9. As can be seen, the calculated response deviates significantly from the cubic fit starting at an incident-field amplitude of ∼5 kV/cm. To explain this noncubic behavior, we note that as seen in Fig. 4, odd harmonics higher than the third harmonic are generally produced; the stimulation of these higher harmonics is due to $\chi^{(5)}$ (and higher) processes, which will not only generate higher harmonics, but will produce an effective $\chi^{(3)}$ that depends upon the field intensity [51]. This results in a lower-than-expected third-harmonic response at higher field intensities. For transmitted field amplitudes up to ∼5 kV/cm, we find (not shown) that the fifth-harmonic response is less than 0.5% of the third harmonic for the 105 meV case, but at

field amplitudes above this the fifth-harmonic field increases more rapidly than the third harmonic. This change occurs at the same field amplitude at which the departure from the cubic prediction is observed in Fig. 9, and these simultaneous changes are observed in all cases examined. At a transmitted field amplitude of 10 kV/cm, the fifth harmonic is nearly 5% of the third harmonic for the 105 meV Fermi level. It is thus clear that the total nonlinear response is beyond a conventional perturbative model, such as that used in Ref. [15]. This means that perturbative models will generally overestimate the third-harmonic generation and that full dynamic simulations such as we perform here are necessary.

V. CONCLUSION

In this paper, we have modeled the third-harmonic response of graphene to single-cycle THz radiation using a nonlinear dynamic model in the length gauge. We have found that for any combination of field amplitude and scattering time, the relative third-harmonic amplitude can be optimized by selecting the correct Fermi level. We simulated the response employing three different types of Fermi-energy-dependent scattering and found that the optimum Fermi energy is strongly influenced by the type of scattering that is dominant in the sample. We have found that the optimization of the Fermi level is very important as a 150 meV deviation in the Fermi energy from the optimum value can reduce the third-harmonic amplitude by a factor of 2 or more.

For all different scattering mechanisms considered, the optimized third harmonic increases subcubically with the incident field due to nonlinear processes beyond third order. This result partially explains the difficulty that researchers have had in observing third-harmonic generation in monolayer graphene and demonstrates the need to employ a nonperturbative approach to the calculation of the nonlinear response of graphene. Future experiments seeking to generate a third-harmonic THz response thus need to consider carefully the scattering rates, the scattering mechanisms, and the Fermi energy if they wish to observe and maximize the third-harmonic response arising from monolayer graphene.

ACKNOWLEDGMENTS

The authors would like to acknowledge the Natural Sciences and Engineering Research Council of Canada (NSERC) for financial support and thank J. E. Sipe for many useful discussions related to the theoretical model.

[1] S. A. Mikhailov, Europhys. Lett. **79**, 27002 (2007).
[2] E. Hendry, P. J. Hale, J. Moger, A. K. Savchenko, and S. A. Mikhailov, Phys. Rev. Lett. **105**, 097401 (2010).
[3] T. Gu, N. Petrone, J. F. Mcmillan, A. V. D. Zande, M. Yu, G. Q. Lo, D. L. Kwong, J. Hone, and C. W. Wong, Nat. Photonics **6**, 554 (2012).
[4] M. Glazov and S. Ganichev, Phys. Rep. **535**, 101 (2014).
[5] K. S. Novoselov, A. K. Geim, S. V. Morozov, D. Jiang, Y. Zhang, S. V. Dubonos, I. V. Grigorieva, and A. A. Firsov, Science **306**, 666 (2004).
[6] S.-F. Shi, T.-T. Tang, B. Zeng, L. Ju, Q. Zhou, A. Zettl, and F. Wang, Nano Lett. **14**, 1578 (2014).
[7] A. H. Castro Neto, N. M. R. Peres, K. S. Novoselov, A. K. Geim, and F. Guinea, Rev. Mod. Phys. **81**, 109 (2009).
[8] S. Das Sarma, S. Adam, E. H. Hwang, and E. Rossi, Rev. Mod. Phys. **83**, 407 (2011).
[9] S. A. Mikhailov and K. Ziegler, J. Phys.: Condens. Matter **20**, 384204 (2008).
[10] A. R. Wright, X. G. Xu, J. C. Cao, and C. Zhang, Appl. Phys. Lett. **95**, 072101 (2009).
[11] M. Dragoman, D. Neculoiu, G. Deligeorgis, G. Konstantinidis, D. Dragoman, A. Cismaru, A. A. Muller, and R. Plana, Appl. Phys. Lett. **97**, 093101 (2010).
[12] K. L. Ishikawa, Phys. Rev. B **82**, 201402 (2010).
[13] F. H. M. Faisal, J. Phys. B: At. Mol. Opt. Phys. **44**, 111001 (2011).
[14] I. Al-Naib, J. E. Sipe, and M. M. Dignam, Phys. Rev. B **90**, 245423 (2014).
[15] J. L. Cheng, N. Vermeulen, and J. E. Sipe, New J. Phys. **16**, 053014 (2014).
[16] H. K. Avetissian, A. K. Avetissian, G. F. Mkrtchian, and K. V. Sedrakian, Phys. Rev. B **85**, 115443 (2012).
[17] S. A. Mikhailov, Phys. Rev. B **90**, 241301 (2014).
[18] N. Kumar, J. Kumar, C. Gerstenkorn, R. Wang, H.-Y. Chiu, A. L. Smirl, and H. Zhao, Phys. Rev. B **87**, 121406 (2013).
[19] S.-Y. Hong, J. I. Dadap, N. Petrone, P.-C. Yeh, J. Hone, and R. M. Osgood, Jr., Phys. Rev. X **3**, 021014 (2013).
[20] P. Bowlan, E. Martinez-Moreno, K. Reimann, T. Elsaesser, and M. Woerner, Phys. Rev. B **89**, 041408 (2014).
[21] M. J. Paul, Y. C. Chang, Z. J. Thompson, A. Stickel, J. Wardini, H. Choi, E. D. Minot, T. B. Norris, and Y.-S. Lee, New J. Phys. **15**, 085019 (2013).
[22] E. H. Hwang, S. Adam, and S. Das Sarma, Phys. Rev. Lett. **98**, 186806 (2007).
[23] E. H. Hwang and S. Das Sarma, Phys. Rev. B **77**, 195412 (2008).
[24] X. Hong, K. Zou, and J. Zhu, Phys. Rev. B **80**, 241415 (2009).
[25] J.-H. Chen, C. Jang, S. Xiao, M. Ishigami, and M. S. Fuhrer, Nat. Nanotechnol. **3**, 206 (2008).
[26] S. Reich, J. Maultzsch, C. Thomsen, and P. Ordejón, Phys. Rev. B **66**, 035412 (2002).
[27] C. Aversa and J. E. Sipe, Phys. Rev. B **52**, 14636 (1995).
[28] E. I. Blount, *Solid State Physics: Advances in Research and Applications* (Academic, New York, 1962), pp. 305–373.
[29] K. S. Virk and J. E. Sipe, Phys. Rev. B **76**, 035213 (2007).
[30] W.-K. Tse, E. H. Hwang, and S. Das Sarma, Appl. Phys. Lett. **93**, 023128 (2008).
[31] I.-T. Lin and J.-M. Liu, IEEE J. Sel. Top. Quantum Electron. **20**, 8400108 (2014).
[32] T. Fang, A. Konar, H. Xing, and D. Jena, Phys. Rev. B **84**, 125450 (2011).
[33] X. Li, E. A. Barry, J. M. Zavada, M. B. Nardelli, and K. W. Kim, Appl. Phys. Lett. **97**, 082101 (2010).
[34] T. Ando, J. Phys. Soc. Jpn. **75**, 074716 (2006).

[35] E. H. Hwang, B. Y.-K. Hu, and S. Das Sarma, Phys. Rev. B **76**, 115434 (2007).
[36] M. I. Katsnelson, F. Guinea, and A. K. Geim, Phys. Rev. B **79**, 195426 (2009).
[37] Y.-W. Tan, Y. Zhang, K. Bolotin, Y. Zhao, S. Adam, E. H. Hwang, S. Das Sarma, H. L. Stormer, and P. Kim, Phys. Rev. Lett. **99**, 246803 (2007).
[38] M. Trushin and J. Schliemann, Europhys. Lett. **83**, 17001 (2008).
[39] V. Ugarte, V. Aji, and C. M. Varma, Phys. Rev. B **84**, 165429 (2011).
[40] T. J. Parker, J. E. Ford, and W. G. Chambers, Infrared Phys. **18**, 215 (1978).
[41] A. P. Zhilinskii, A. P. Gorchakov, T. S. Egorova, and N. A. Miskinova, Opt. Spectrosc. **62**, 783 (1987).
[42] C. M. Randall and R. D. Rawcliffe, Appl. Opt. **6**, 1889 (1967).
[43] C. J. Docherty, C.-T. Lin, H. J. Joyce, R. J. Nicholas, L. M. Herz, L.-J. Li, and M. B. Johnston, Nat. Commun. **3**, 1228 (2012).
[44] Due to the Gaussian envelope, for a single-cycle pulse with a central frequency of 1 THz and a full width at half maximum of 1 ps, the actual peak field is 86% of E_o.
[45] J. Hebling, G. Almási, and I. Z. Kozma, Opt. Express **10**, 1161 (2002).
[46] K. Tanaka, H. Hirori, and M. Nagai, IEEE Trans. Terahertz Sci. Technol. **1**, 301 (2011).
[47] P. U. Jepsen and B. M. Fischer, Opt. Lett. **30**, 29 (2005).
[48] R. Piesiewicz, C. Jansen, S. Wietzke, D. Mittleman, M. Koch, and T. Kürner, Int. J. Infrared Millimeter Waves **28**, 363 (2007).
[49] H. A. Hafez, I. Al-Naib, K. Oguri, Y. Sekine, M. M. Dignam, A. Ibrahim, D. G. Cooke, S. Tanaka, F. Komori, H. Hibino, and T. Ozaki, AIP Adv. **4**, 117118 (2014).
[50] H. A. Hafez, I. Al-Naib, M. M. Dignam, Y. Sekine, K. Oguri, F. Blanchard, D. G. Cooke, S. Tanaka, F. Komori, H. Hibino, and T. Ozaki, Phys. Rev. B **91**, 035422 (2015).
[51] This is similar to the Kerr effect on the effective index of refraction in a $\chi^{(3)}$ material, but it occurs at a higher order.